FULL PAPER

Compressed Perovskite Aqueous Mixtures Near Their Phase Transitions Show Very High Permittivities: New Prospects for High-Field MRI Dielectric Shimming

Ana L. Neves ⓘ,[1,2] Lisa Leroi,[3] Zo Raolison,[3] Nicolas Cochinaire,[1] Thibaut Letertre,[1] Redha Abdeddaïm,[1] Stefan Enoch,[1] Jerome Wenger,[1] Johann Berthelot,[1] Anne-Lise Adenot-Engelvin,[4] Nicolas Malléjac,[4] Franck Mauconduit,[5] Alexandre Vignaud,[3] and Pierre Sabouroux[1]*

Purpose: Perovskites are greatly used nowadays in many technological applications because of their high permittivity, more specifically in the form of aqueous solutions, for MRI dielectric shimming. In this study, full dielectric characterizations of highly concentrated $CaTiO_3/BaTiO_3$ water mixtures were carried out and new permittivity maxima was reached.
Methods: Permittivity measurements were done on aqueous solutions from 0%v/v to dry powder. The permittivity dependence with pressure was investigated. Scanning electron microscopy images were performed on a few representative solutions. $BaTiO_3$ pressed pads of different thicknesses, permittivities, and distances to the head were compared in a 7T MRI scanner.
Results: Perovskite aqueous mixtures undergo a pressure-dependent phase transition in terms of permittivity, with increasing water content. A new relative permittivity maximum of 475 was achieved. Microscopic images revealed structural differences between phases. A B_1^+ improvement in the temporal lobe was obtained with thin, high permittivity $BaTiO_3$ head.
Conclusions: This new preparation method allows improved pad geometry and placement, as a result of the high relative permittivity values achieved. This method has great significance for medical applications of MRI dielectric shimming, being easy to replicate and implement on a large scale.
**Magn Reson Med 000:000–000, 2017. © 2017 The Authors Magnetic Resonance in Medicine published by Wiley Periodicals, Inc. on behalf of International Society for Magnetic Resonance in Medicine. This is an open access

[1]Aix Marseille Univ, CNRS, Centrale Marseille, Institut Fresnel, Marseille, France.
[2]Centre Commun de Ressources en Micro-ondes, IUSTI – Tech. de Château-Gombert, Marseille, France.
[3]CEA, DRF/ISVJF/Neurospin, Gif-sur-Yvette Cedex, France.
[4]CEA–DAM Le Ripault, Monts, France.
[5]Siemens Healthineers, Saint Denis, France.

*Correspondence to: Pierre Sabouroux, Ph.D., Institut Fresnel, CNRS, Aix-Marseille Université, Ecole Centrale Marseille, Faculté des Sciences Saint-Jérôme, 52 Av. Escadrille Normandie-Niémen, 13013 Marseille, France. Tel: (+33) 4 91 28 83 53; E-mail: pierre.sabouroux@fresnel.fr.

INTRODUCTION

High permittivity perovskite composites have been largely studied in the past few years, mostly because of their innumerous technological applications (1). These electromagnetic materials are highly demanded nowadays (2,3). The perovskite barium titanium oxide ($BaTiO_3$) is a dielectric microwave material greatly used in the electronic industry; applications in several fields can be stated, such as in (i) multilayer, high-capacity capacitors and dielectric resonator antennas, resulting from high permittivities with few losses at a given frequency; (ii) in thermometers and infra-red detectors, considering the thermic sensitivity; (iii) in motion, pressure and humidity sensors, owing to piezo-electricity; and (iv) in frequential filters, medical imaging, and antiradar surfacing (4–8). Research has been led to improve the production methods to achieve the most auspicious features in novel structures (9,10), in fine nanoparticles (11–13), and additionally in increasing the dielectric constant (14). Moreover, new composite materials based on titanate powders mixed with a polymer matrix are currently being developed for 3D-printing devices such as antennas (15), despite the lowering of the relative permittivity from values higher than 1000 to 4 to 5, as a result of depolarizing effects in the composite medium. Although this class of composites offers great opportunities in terms of processing the material at a low cost, it is not suited for high permittivity applications.

Nowadays, one of the most prominent applications of perovskites is in the domain of high-field MRI, in dielectric shimming processes—the purpose of which is to generate a more homogenous radiofrequency (RF) magnetic field. The concept of a dielectric resonator was first adapted to MRI by Alsop et al (16), and later on by Wen et al (17) and Yang et al (18), who explored this concept by using water pads placed in specific configurations

around the body to manipulate the RF field; later, these pads were replaced by titanate-water saturated mixtures (19–21), in which the feasibility and increased performance of the procedure in the presence of $BaTiO_3$ and calcium titanium oxide ($CaTiO_3$) were demonstrated: The high dielectric polarizability of titanate compounds enhances the permittivity of the water. The development of these pads is currently a subject of research, and the optimization of thickness, size, geometry and permittivity, needed for specific applications, is still required (22–25). Additionally, in certain occasions, the fluidity of the pad solution can cause it to deform and disturb the spatial distribution when placed under the patient (20,21).

The adjustment of the permittivity of perovskite mixtures to very specific values has been reported very little in the literature; usually, the suspensions are prepared to obtain a saturation point, which has been reported to correspond to the highest permittivity values of both $CaTiO_3$ and $BaTiO_3$ (19–21,26). It remains unclear whether higher permittivity values can be found when exploring lower water concentrations, thus beyond the saturation point.

Recently, the use of $BaTiO_3$ slurries of sintered beads was proven to be suitable for dielectric shimming pads, identically to slurries of $BaTiO_3$ powder; in the case of beads, relative permittivity values were reported to reach up to 487, as opposed to 319 (the case of powder slurries) at 300 MHz (27). Nonetheless, the most currently used solutions for dielectric shimming are aqueous mixtures of $CaTiO_3$ and $BaTiO_3$ powders, which permittivities do not exceed 110 and 300, respectively (19,21,26). These values are a result of powder-saturated solutions of approximately 45 to 50% v/v.

Therefore, this study aims to assess the dielectric influence of water ranging from 0 to 100% v/v in the perovskite powders $BaTiO_3$ and $CaTiO_3$, from 50 to 800 MHz. More specifically, by using commercially available perovskites, we are looking for the highest permittivity values achievable when preparing dielectric shimming solutions, independently of the saturated nature of the suspension. Pressure appears to have a great influence on the dielectric constant of very saturated perovskite mixtures, resulting in extremely high permittivities, especially in the case of $BaTiO_3$; thus, the effect of several machine-pressed $BaTiO_3$ pads of different thicknesses and placed at different distances were tested on two phantoms in a 7T MRI system. The determination of two mathematical rules (two-phase Lichtenecker's logarithmic power law and three-phase coherent potential approximation), which describe completely the behavior of the permittivity of the mixtures as a function of the water content (without any restriction of the volume fraction), is very important to control the effect of the pad in clinical applications.

METHODS

Permittivity Measurements

The permittivity of $BaTiO_3$ (barium titanium oxide, 99% metals basis, 12348, Alfa Aesar, Averhill, MA) and $CaTiO_3$ (calcium titanium oxide, 99+% metals basis, 11397, Alfa Aesar) aqueous mixtures were characterized. The estimated density of $CaTiO_3$ powder is $4.1 \, g/cm^3$ (28)

and of $BaTiO_3$ powder is $5.85 \, g/cm^3$ (29), both having a particle size of less than $44 \, \mu m$ (-325 mesh powder).

To perform the microwave characterization of the mixtures, a reflexion/transmission technique (30,31) using a coaxial cell with sample holder (Fig. 1a) is used. The measurement process is based on the S-parameter acquisition of the cell with the integrated sample; then, through a de-embedding process and the Nicolson-Ross algorithm (32), the complex permittivity of the sample is determined (33). The complex relative permittivity is denoted in Equation [1], where ε' represents the real part of permittivity and ε' represents the imaginary part of permittivity.

$$\varepsilon^* = \varepsilon' - j\varepsilon'' \qquad [1]$$

Having these values, it is possible to determine the dielectric loss as follows:

$$\tan \delta = \frac{\varepsilon''}{\varepsilon'} \qquad [2]$$

The coaxial cell has a sample confinement zone defined by two dielectric partitions, with a net volume of $0.65 \pm 0.02 \, cm^3$, and two millimetric cavities allowing an access for circulating liquids (the volume error is determined considering the dimensions of the confinement zone). A real-time characterization of both dilute solutions and extremely saturated solutions is possible. Those results are not altered by uncertainties that may originate from the use of two different measurement methods.

The perovskite powder was dried in a moisture analyzer (MJ33, Mettler-Toledo, Columbus, OH) before any manipulation. The base moisture content (MC) of the powder provided by the manufacturer ranged from 0.08 to 0.15% MC. The permittivity of both perovskites dry powder was measured.

The liquid access of the cell was used to measure the solution from 0% v/v (pure water) until approximately 50% v/v. A continuous flow of liquid inside the cell's confinement area is achieved through a connection to a peristaltic pump and a beaker containing the solution, which is continuously stirred (Fig. 1b). A beaker with pure distilled water (SAJ-07-6061, Sigma-Aldrich, St. Louis, MO) was placed on the setup, and a first measurement was acquired. Then, a specific amount of powder was added and the permittivity of the mixed homogeneous solution was measured. The procedure was repeated at regular intervals, until the 1:1 ratio was reached. At this point the solution becomes saturated, so the liquid access can no longer be used.

In a second stage, a predetermined amount of distilled water was added to a new sample of completely dry powder, manually inserted into the confinement area, and measured with the coaxial cell. A few samples were prepared, now by applying $2 \, tons/cm^2$ to the confinement area (Fig. 1c), thus highly compressing the mixture inside the cell. A hydraulic machine press was used at this point. After the permittivity measurement, the water content of all samples was measured in the moisture analyzer, for an accurate quantification of the water fraction.

The results were compared with two known mixing rules. First, to describe the permittivity of the perovskite solutions in the 0 to 60% v/v regime, a two-phase Lichtenecker's logarithmic power law was used, as follows (19,20,26,34):
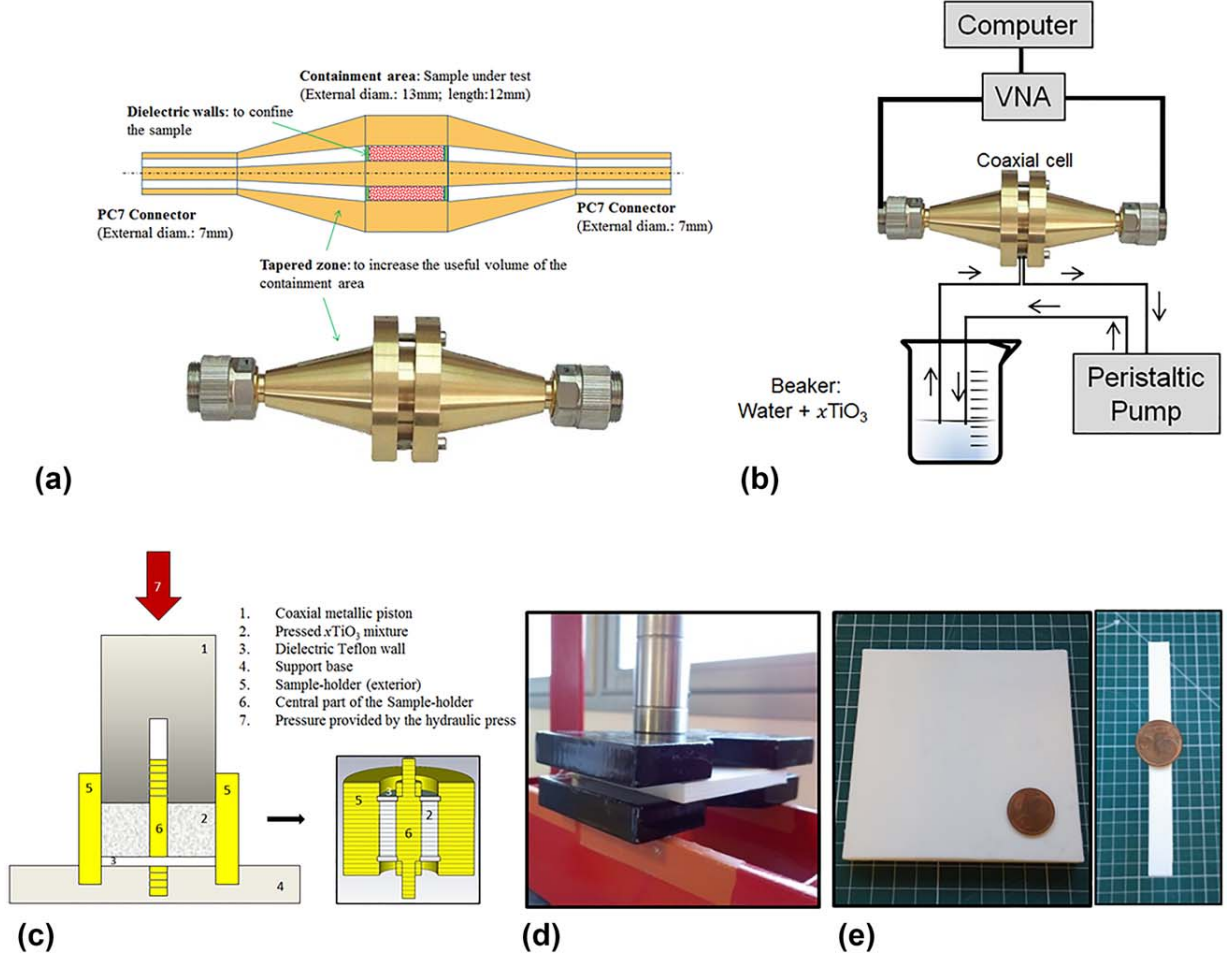
FIG. 1. **a**: Schematic figure of the cell, displaying the confinement area for solids and liquids in the center, and the internal structure of the coaxial cell, and PC7 connectors (top) and the coaxial cell (bottom). **b**: The experimental setup with the coaxial cell for liquid samples (>50% v/v). The solution in constant stirring will circulate inside the coaxial cell by means of a peristaltic pump. The software will retrieve the S-parameters displayed in the Vector Network Analyzer, which is connected to the coaxial cell, and displays the dielectric properties of the sample. **c**: Schematic illustration of the pressing method and closed sample-holder with mixture after pressing. **d**: Photograph of the mixture being pressed inside a 5-mm-thick PLA box (in white) with the help of two blocks to distribute the weight (in black). **e**: Front and side view of Pad E (5 mm thick) (Supporting Table S1).

$$\varepsilon_{\text{eff}} = \prod_{i}^{N} \varepsilon_i^{f_i} \qquad [3]$$

where ε_{eff} is the effective permittivity of the mixture, ε_i is the permittivity of each component, and f_i is the volume fraction of each component of the mixture.

The coherent potential approximation (CPA) law proposed by Sen et al [35] was compared with the results from 60 to 100% v/v (Eq. [4]). Because both perovskites have a comparable granulometry, the air/powder fractions are very similar for the same water-content points:

$$\sum_{i} f_i \left[\frac{\varepsilon_{\text{eff}} - \varepsilon_i}{2\varepsilon_{\text{eff}} + \varepsilon_i} \right] = 0 \qquad [4]$$

The used permittivity values were $\varepsilon_{\text{CaTiO3}} = 160$ (21,26) and $\varepsilon_{\text{BaTiO3}} = 1200$ (36), and $\varepsilon_{\text{water}} = 79$ (37) and $\varepsilon_{\text{air}} = 1$ (38).

All permittivity measurements were performed from 50 to 800 MHz at room-temperature conditions (19 °C, 41% humidity). All weight measurements were made with a Mettler-Toledo scale of error 0.01, and the water content was determined with a moisture analyzer of error 0.01. The standard deviation associated with the measurements was approximately 5% for all frequencies.

Scanning Electron Microscope Imaging

To evaluate the microscopic behavior of mixtures having different consistencies, eight samples were imaged with a scanning electron microscope (SEM): (i) dry BaTiO$_3$, (ii) 63.5% v/v BaTiO$_3$, (iii) 46.5% v/v BaTiO$_3$, (iv) 74.2% v/v BaTiO$_3$ (the latter uncompressed), and (v) a 72.9% v/v BaTiO$_3$ pressed sample. CaTiO$_3$ samples with similar water contents were also imaged. Because both perovskites behave similarly for equivalent water contents, we chose to display only the BaTiO$_3$ results. Images were performed on a FEI DB235 microscope (Hillsboro, OR) with a field emission gun. The spatial resolution was 5 nm at 5-kV acceleration voltage.
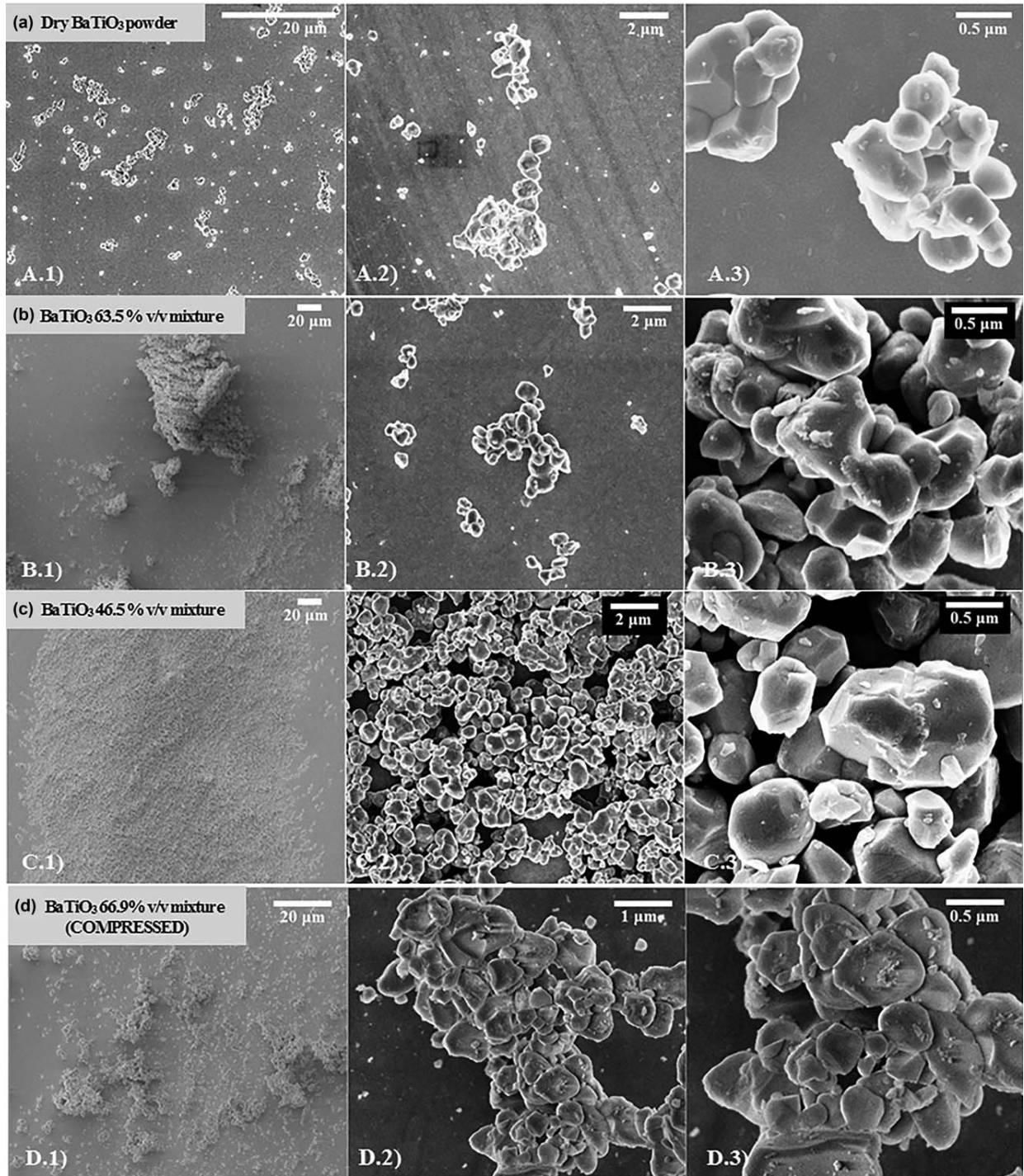
FIG. 2. Scanning electron microscope images of three different resolutions (20 μm (1), 1 or 2 μm (2), and 0.5 μm (3)) of dry $BaTiO_3$ powder (**a**), 63.5% v/v $BaTiO_3$ (**b**), 46.5% v/v $BaTiO_3$ (**c**), and a compressed $BaTiO_3$ mixture of 66.9% v/v (similar water content as the uncompressed samples b.1 to b.3) (**d**).

Magnetic Resonance Imaging Experiment

Calcium titanate has a maximal reported relative permittivity of 150 to 160 (bulk), whereas barium titanate can achieve greater values (its bulk relative permittivity has been reported up to 10000, depending on grain size and sintering process) (26). Therefore, for a 7T MRI pad evaluation, mixtures of $BaTiO_3$ were preferred over $CaTiO_3$. Thus, six $BaTiO_3$ uncompressed and machine-pressed (Figs. 1d and 1e) pads of $10 \times 10 \, cm^2$ were prepared, having different thicknesses (Supporting Table S1). To this end, polylactic-acid (PLA) containers ($\varepsilon' \sim 3$) were 3D printed. The largest container was 10 mm thick
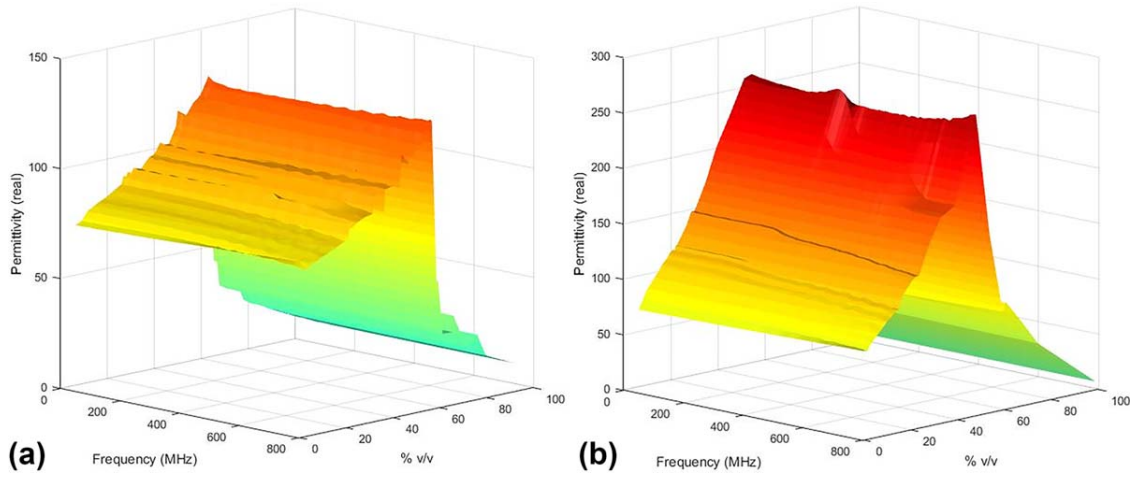
FIG. 3. Real part of permittivity as function of frequency and MC for uncompressed $CaTiO_3$ samples (**a**) and $BaTiO_3$ samples (**b**).

(Pad F) and had the highest pressure resistance, consequently making it possible to attain higher densities and permittivities in the mixture. The other 2-mm-thick containers did not support high pressures and risked breaking more easily (Pads C, D, and E). The uncompressed pads were placed in polypropylene flexible containers (Pads A and B). To determine ε^*, a small sample of each pad was collected, and the water content was confirmed in the moisture analyzer.

Validation experiments were performed using a birdcage head coil 1Tx/1Rx (Invivo Corp, Gainesville, FL) and a home-made spherical 3% agarose phantom (of $\varepsilon_r = 74.2$ and $\sigma = 0.87$ S/m) in a 7T Magnetom MRI scanner (Siemens Healthineers, Erlangen, Germany). B_1^+ maps were acquired through flip-angle imaging (AFI) sequence (39) measurements of the phantom only (control) and, consecutively, of the phantom with Pads A, B, D, and F placed on the right side. To mimic the PLA container of Pad F, the other pads were separated from the phantom by a 1-cm-thick PLA spacer.

To evaluate the trade-off among pad thickness, permittivity, and distance to the head, three sets of pad configurations were explored with a specific anthropomorphic mannequin (SAM) head phantom (SPEAG, Zürich, Switzerland). First, using the same birdcage head coil, B_1^+ maps were acquired through AFI sequence measurements of pads of different thicknesses $\underline{e}$, adjacent to the phantom. To do so, Pad E (5 mm thick), Pad C (10 mm thick), and finally both pads (10 + 5 mm) were placed adjacent to the head (10-mm pad adjacent to the phantom). The latter case is not ideal, and may not provide an accurate comparison with the other two cases, as a one-piece pad of 15 mm may not behave similarly as adjacent pads of 10 + 5 mm.

With the same setup, B_1^+ maps were acquired on the phantom alone and on the phantom with Pad E (5 mm thick) placed at an increasing distance $\underline{d}$ of 0, 5, 10, and 20 mm from the right side of the head.

The final setup consisted of determining the influence of pad permittivity on the field distribution; thus, B_1^+ maps were acquired by placing a lower permittivity pad, Pad C (10 mm, $\varepsilon' = 241$), adjacent to the phantom.

Field Simulations

CST Microwave Studio B_1^+ maps (Computer Simulation Technology, Framingham, MA) of a spherical phantom and a shielded birdcage head coil, having 16 double rungs of 18 cm each with a diameter of 0.4 cm, and 16 capacitors of 6 pF, were simulated for the five pad-configuration cases. The simulated birdcage coil had a broadband excitation between 200 and 400 MHz, and was designed to resonate at 300 MHz when charged; no retune or rematch was done when inserting the pads.

The same procedure was performed using CST Voxel Family's adult male head of "Gustav" inside the birdcage coil, to obtain the global specific absorption rate (SAR) and maximal local SAR with pads of different thickness, permittivity, and distance to the head. In this case, global SAR corresponds to the SAR averaging over the whole head, and the maximal local SAR corresponds to the maximum in local exposure caused by the inhomogeneity in the RF field, averaged over 10 g of tissue (40).

The SAR calculations in CST were obtained using a power-loss density monitor at 300 MHz, averaging over 10 g of mass, with a stimulated power of 2 W and one excitation signal of 20.5 ns. For this analysis, the pads were placed centered on the right ear of the Gustav head model.

RESULTS

The SEM images of dry $BaTiO_3$ powder reveal scattered particles having a diameter no bigger than 1 μm, barely forming aggregates (Fig. 2a). In the intermediate stage from 60 to 99% v/v, in which macroscopically the sample is perceived as crumbly, it is possible to notice the presence of larger aggregates (no larger than 20 μm in diameter) and less scattered particles (Fig. 2b). Finally, when considering the liquid perovskite mixture (Fig. 2c), the particles are entirely aggregate, forming a film of mixture when placed on the sample support.

As for the permittivity of the samples, ε' values are quite constant throughout the frequency range, showing a coefficient of variation of less than 0.029 in the case of $CaTiO_3$ and of less than 0.064 in the case of $BaTiO_3$—as
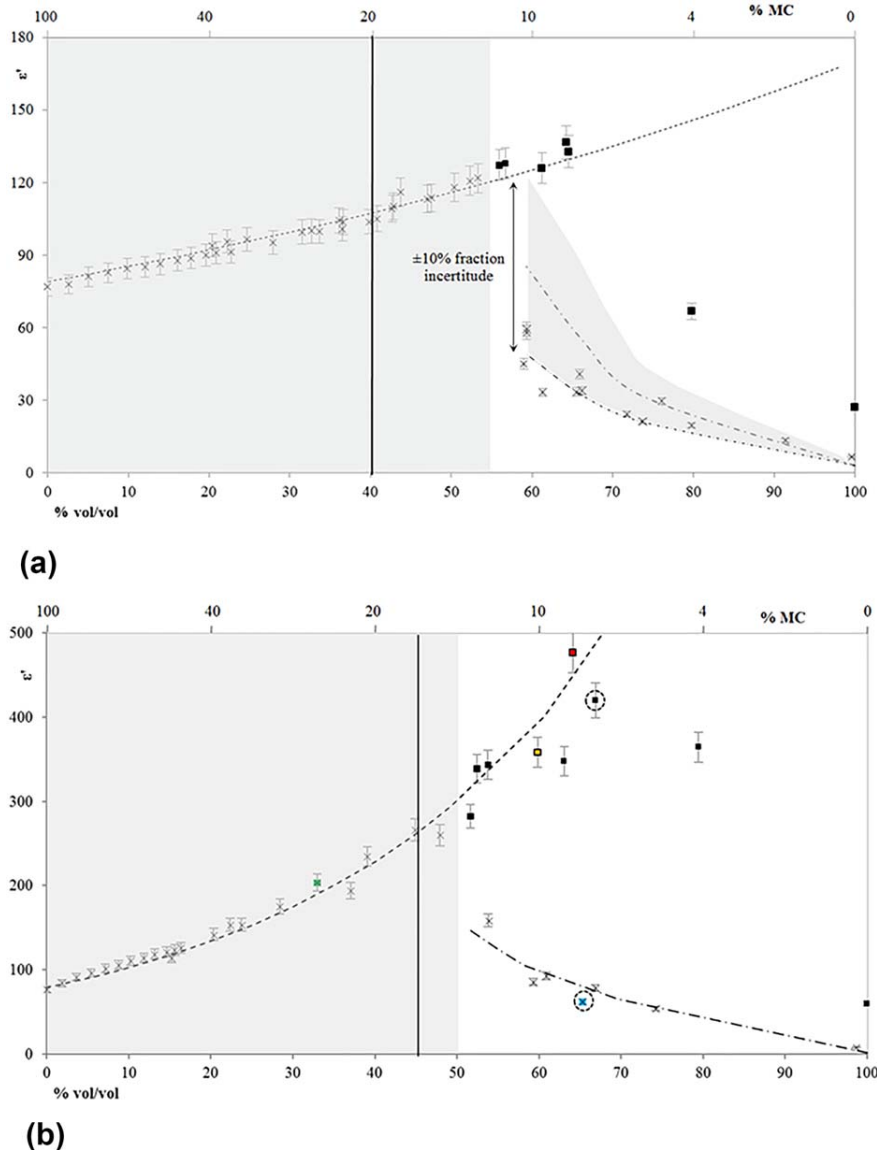
(a)

(b)

FIG. 4. Real part of permittivity as a function of water content (% v/v on the bottom horizontal axis and % MC on the top horizontal axis) at 300 MHz, for $CaTiO_3$ (**a**) and $BaTiO_3$ (**b**) solutions manually (x) and machine-pressed (■), as well as the two-phase Lichtenecker's logarithmic power law (-----) represented at the first stage (gray area), and three-phase CPA law (— ·· —) represented at the second stage (white area). The black vertical lines refer to the maximal water content reported in the literature (21). In the case of $CaTiO_3$, the CPA law is shown calculated with the original air and powder fractions (dashed gray curve), and also calculated by taking into account a $\pm10\%$ uncertainty associated with the measurement devices, which influence the air and powder fractions. When considering a 10% reduction in the air fractions (dashed and dotted black curve), the CPA law is found to agreeably integrate the experimental data. The two dashed circles represent the samples shown in Figure 2d. The four colored points correspond to the pads tested in the 7T MRI (corresponding to the colored frames in Fig. 6c).

shown in Figure 3A for $CaTiO_3$ and Figure 3b for $BaTiO_3$. Therefore, for all frequencies it is possible to consider the same interpretation. Thus, to proceed to a detailed analysis of the data as a function of water content, the complex permittivity of both perovskite mixtures was measured at 300 MHz, a central frequency in the range, and most importantly, the Larmor frequency of ^1H at 7. Figure 4 represents ε' at 300 MHz for $CaTiO_3$ and $BaTiO_3$ (Figs. 4a and 4b, respectively), and Figure 5 represents ε'' and tan δ values for $CaTiO_3$ and $BaTiO_3$ (Figs. 5a and 5b, respectively).

When considering the manually pressed mixtures, both perovskites display the same behavior, which can be separated in two stages. From pure water or 0% v/v, until approximately 60% v/v, the real part of permittivity increases until reaching a maximum. The Lichtenecker's logarithmic power law follows the same behavior in this stage. Here, the samples have a liquid consistency and consist of a water and a powder phase.

Afterward, from 60 until 100% v/v, ε' decreases from the maximum value until reaching the permittivity of dry powder. The volume fraction of water at each point is known through the MC value given by the moisture analyzer. The volume fraction of perovskite powder is estimated through the measured mass of each sample and the density of the perovskite. The total volume of the confinement zone is estimated to be $0.65 \pm 0.02\,cm^3$. The volume fraction of air is a delicate element to calculate; it is estimated in the range of 20.1 to 77.2% (bearing in mind a certain error margin), associated with the determination of the confinement zone volume, mass of the sample, and moisture analysis.

Consequently, Figure 4a ($CaTiO_3$ case) plots the two three-phase CPA laws: (i) a curve determined by using the originally calculated air fractions, and (ii)
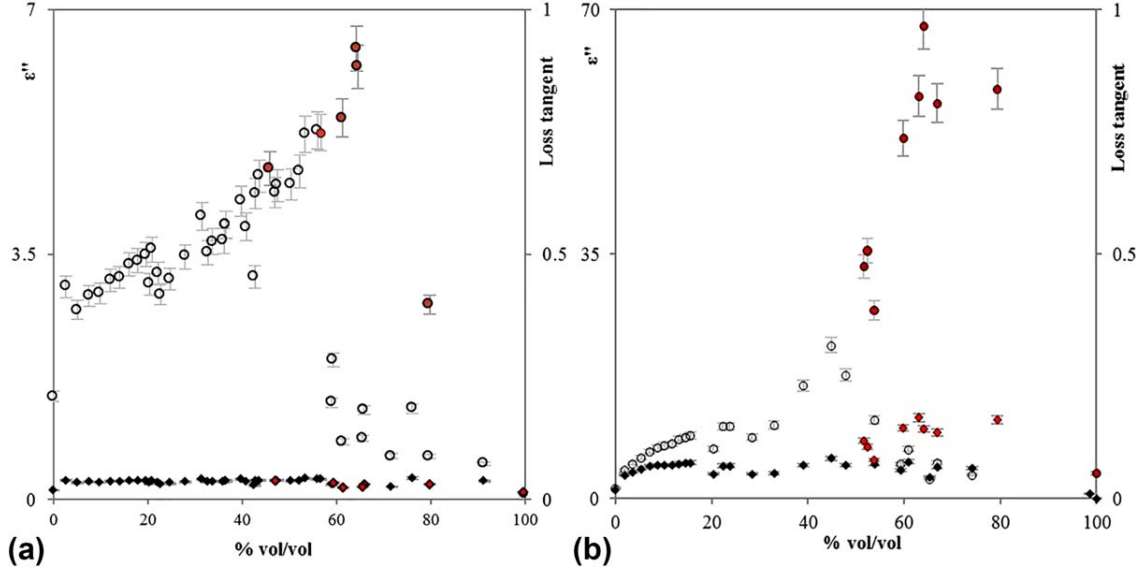
FIG. 5. Imaginary part of permittivity, pressed (●) and uncompressed (○), and loss tangent for pressed (◆) and uncompressed (◆) for the CaTiO$_3$ samples (**a**) and BaTiO$_3$ samples (**b**), as a function of water content.

considering a 10% error overestimation presumably done on these air fractions. When calculating the CPA law with a 10% decrease in the air fractions (relatively to the originally calculated), the law shows a good agreement with the experimental data. If considering these 10% discrepancy air fractions into the CPA law for BaTiO$_3$, a

good correspondence is also found. We stress that these laws are not numerical interpolations of the experimental data; they are based on a physical model in which all parameters are known.

In the cases in which pressure is applied with the hydraulic machine press, no significant change occurs in
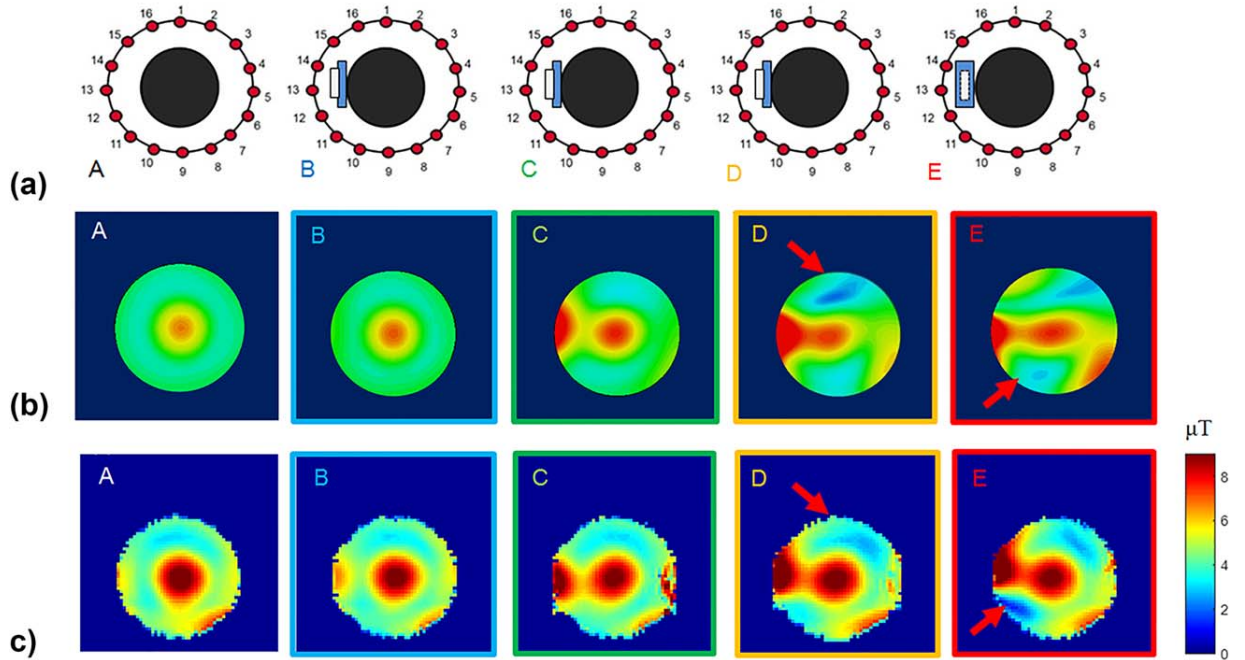

FIG. 6. **a**: Schematic representation of BaTiO$_3$ pad positioning inside the birdcage head coil. **b**: CST Microwave Studio simulation of B$_1^+$ map of the phantom inside the birdcage head coil. **c**: Transversal plane of B$_1^+$ map, obtained with AFI on an agarose homemade phantom. The five cases correspond to: a reference scan without pad (A); Pad A with a PLA spacer of 1 cm (B); Pad B with a PLA spacer of 1 cm (C); Pad D with a PLA spacer of 1 cm (D); and Pad F inside a PLA container (E); the red arrows highlight the appearance of destructive interferences. The colored frames correspond to the colored circled points in Figure 4b. The pads were the same size and thickness and were installed on the right side of the phantom (left side of the image).
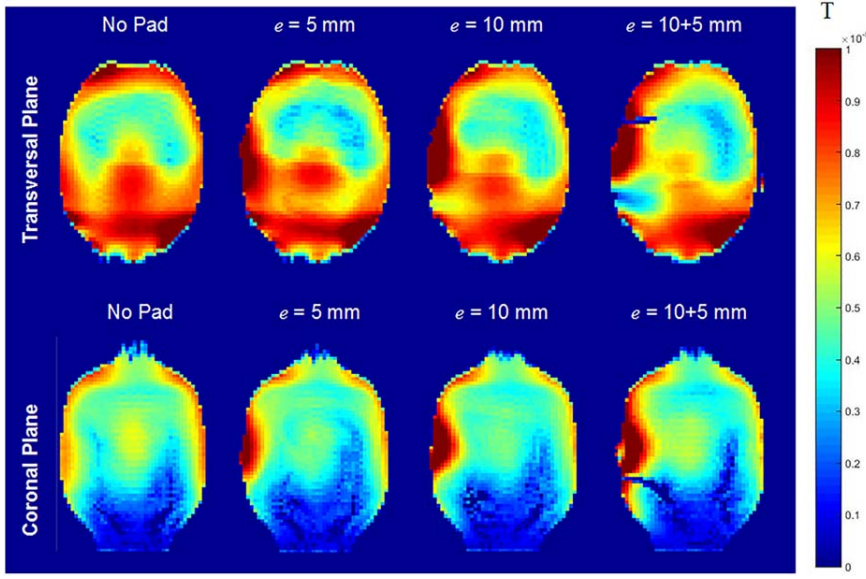
FIG. 7. Transversal plane and coronal plane of B_1^+ map, obtained through AFI sequence measurements on a SAM phantom on four different pad-thickness (e) configurations: no pad (**a**), Pad E adjacent to SAM (**b**), Pad D adjacent to SAM (**c**), and the two previous pads adjacent to each other and to SAM (10-mm pad adjacent to the phantom's ear) (**d**).

the permittivity values of the first stage when compared with a similar manually pressed solution. However, the maximum permittivity point achieved is higher, although slightly shifted to the right for both perovskites. At this point, where the pressed and uncompressed mixtures demonstrate a significant dispersion in terms of permittivity, SEM images were obtained for a similar pressed mixture of $BaTiO_3$ (Fig. 2d). It is possible to identify a great number of flattened-out particles in the pressed case compared with the uncompressed case.

The imaginary part of permittivity follows the same behavior as the real part, although with substantially lower values. Thus, the dielectric loss of the material tanδ, as described in Equation [2], has a significantly constant value throughout the MC range. For uncompressed samples, the average value and standard deviation of the loss tangent is 0.04 ± 0.01 and 0.07 ± 0.03, respectively.

Figure 6a displays a schematic representation of the phantom inside the birdcage head coil, with the adjacent pad. Figure 6b shows the five CST simulated cases, and Figure 6c shows the five corresponding MRI images. The different configurations are a control situation with no pad, then the spherical phantom with Pads A, B, D, and F. Effectively, the field-distribution effects of constant-thickness pad increase proportionally with the permittivity [26,41]. In the case without pad, the B_1^+ lowest value equidistant to the left ear and the center of the head is equal to 4.123 µT; it increases by 15% for Pad A, 44% for Pad B, 67% for Pad D, and by 82% for Pad F. This restoration is better when the permittivity is higher. It is important to notice that the effect of the highest relative permittivity pads becomes unfavorable to a uniform B_1^+ distribution [20], with the appearance of a new dark zone and an unbalanced field repartition (red arrows in Figs. 6b and 6c) instead of compensating for the weak signal area.

Figure 7 shows the B_1^+ map of the first experiment set on pad geometry optimization. It is possible to notice that with increasing pad thickness, the bright area visible on the transversal and coronal left side becomes more

prominent. Nonetheless, the two dark zones present in the transversal plane also become more evident in the presence of thicker pads; on the coronal plane of the $10 + 5$ mm pad case, the areas of lower field begin to encircle the high-field area on the left. It is clear that this case is not identical to a 15-mm-thick pad, but it can provide a first perception of how a large thickness pad may affect the B_1^+ field. The dark zones that appear with increasing thickness compromise the efficacy of the pads for shimming purposes.

Figure 8 displays the B_1^+ field maps as a function of pad distance to the head. Pad E (5 mm thick, $\varepsilon' = 358$), when placed adjacent to the SAM head phantom ($d = 0$ mm), induces a large bright area with high B_1^+ field, visible on the left side of both planes. This field maximum decreases with increasing distance, similar to the dark areas that appear in the presence of the pad on the transversal plane.

Figure 9 displays a comparison between the effects of different permittivity pads on the field distribution. A pad of the same thickness but lower dielectric constant and lower losses like Pad C ($\varepsilon' = 241$, $\varepsilon'' = 29$) generates a slightly weaker field compensation than a pad of the same size but with higher ε^* (Pad D, $\varepsilon' = 348$, $\varepsilon'' = 58$), visible on the transversal plane. On the coronal plane, the difference between the strong effects generated by the pads is very subtle.

To quantify these effects, three significant regions of interest (ROIs) (one on the coronal plane and two on the transversal plane) were chosen to represent the B_1^+ field variation on SAM for each case. These regions were chosen because they include the maximum and minimums in the B_1^+ field. The coronal ROI includes the area where the pad has the highest impact, with an increase in the field whenever present, and the two transversal ROIs encircle the areas where the dark zones appear.

Figures 10a and 10b display the ratio between the transmit B_1^+ field homogeneity with pad and without pad (phantom alone):

FIG. 8. Transversal plane and coronal plane of B_1^+ map, obtained through AFI sequence measurements on a SAM phantom on five different distance (*d*) configurations: no pad (**a**), Pad E ($\varepsilon' = 358$, 5 mm thick) adjacent to SAM (**b**), Pad E distanced 5 mm from SAM (**c**), Pad E distanced 10 mm from SAM (**d**), and Pad E distanced 20 mm from SAM (**e**).
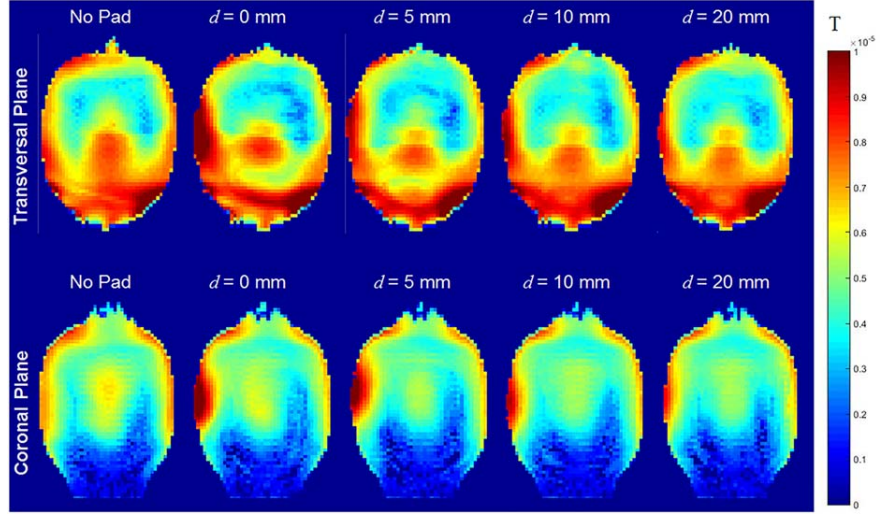
$$\frac{B_1^+ \; field \; average \; in \; ROI \; of \; the \; phantom \; wih \; pad}{B_1^+ \; field \; average \; in \; ROI \; of \; the \; phantom \; alone} \times 100 \quad [5]$$

as a function of pad thickness and as a function of pad distance, respectively. Figures 10c and 10d display the ratio of global SAR and maximal local SAR simulated inside Gustav as a function of pad thickness and pad distance, respectively. The values of global and maximal SAR with pad are presented as a ratio to the global and maximal SAR of the phantom alone. Supporting Figure S1a outlines the three ROIs considered, and Supporting Figure S1b exemplifies the local maximal SAR found on

the three planes for the reference Gustav case, without pad.

When considering pad thickness, the field variation on the coronal ROI (hereafter referred to as CR) with 5-mm and 10-mm-thick pads increased by 68%, as opposed to a 38% with a $10 + 5$-mm-thick pad. Nonetheless, on transversal ROIs 1 and 2 (hereafter referred to as TR1 and TR2), the field decrease is too strong, leading to deep dark zone areas. This is clearly shown in Figure 7, in the case of Pads E and D placed together. Concerning the variation between the dark zones, a 5-mm pad exceptionally shows an increase in the TR2. On TR1, all pads show a

FIG. 9. Transversal plane and coronal plane of B_1^+ map, obtained through AFI sequence measurements on a SAM phantom on three different pad permittivity configurations: no pad (**a**), Pad C (10 mm) adjacent to SAM (**b**), and Pad D (10 mm) adjacent to SAM (**c**).
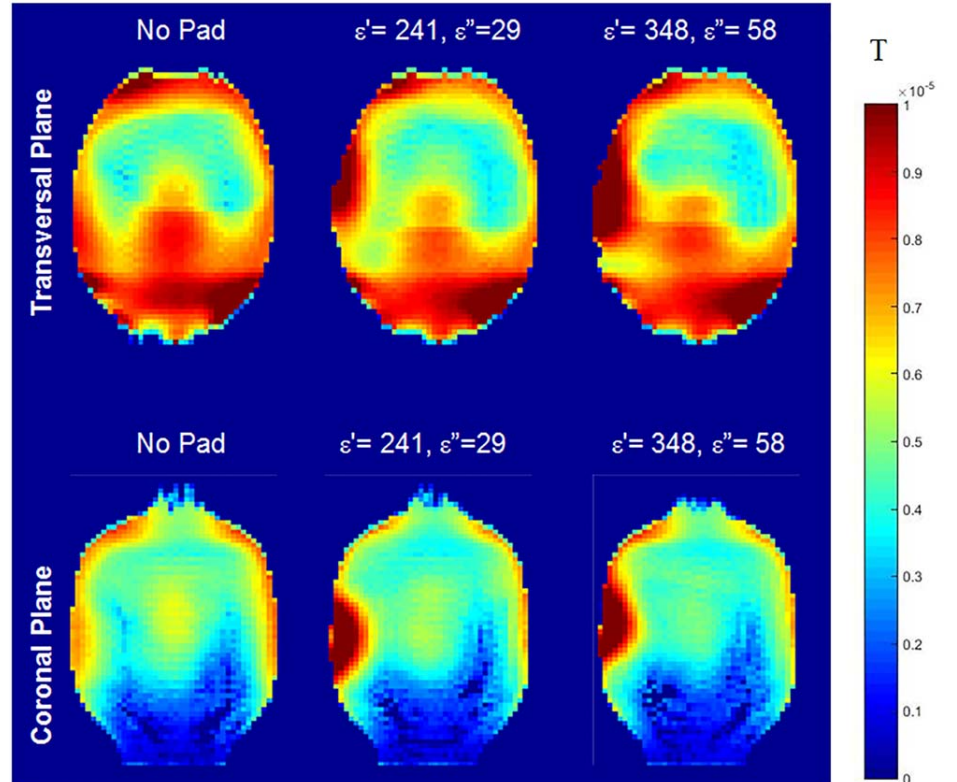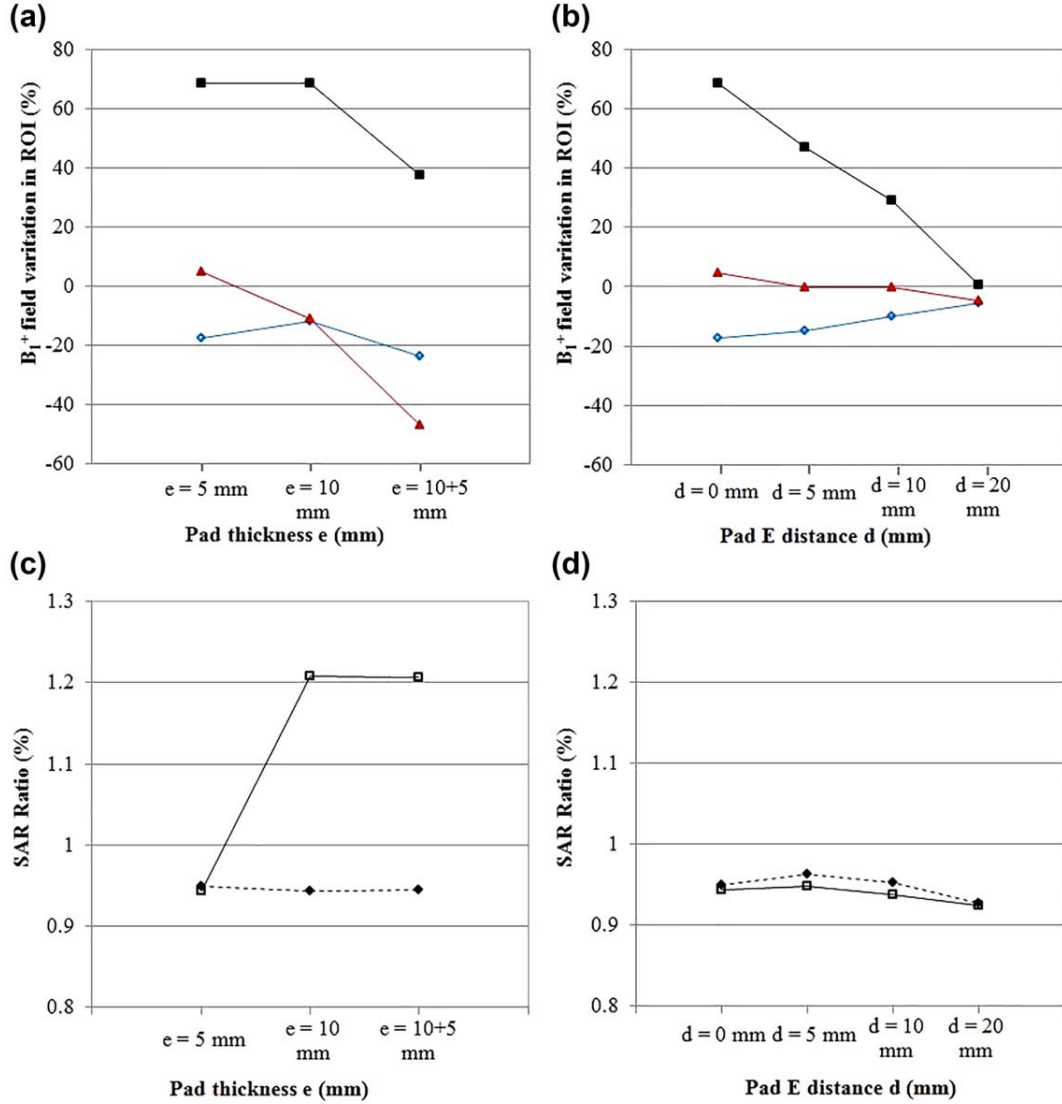
FIG. 10. **a**: B_1^+ field ratio (ratio to the phantom without pad) on CR (■), TR1 (◆), and TR2 (▲) for the three pad-thickness cases. **b**: B_1^+ field variation on CR (■), TR1 (◆), and TR2 (▲) for the four Pad E distance cases. **c**: Global SAR ratio (--◆--) and maximal local SAR ratio (-□-) for the three pad-thickness cases; and global SAR ratio (--◆--) and maximal local SAR ratio (-□-) for the four Pad E distance cases (**d**).

similar decreasing effect. In this set of experiments, the global SAR on the head greatly increases with thicker pads. However, the maximal local SAR on the proximity of the pads does not show a significant variation.

Regarding pad distance to the head, the strong field effects present on the CR decrease linearly with increasing distance. When distancing the pad by 20 mm, these are barely visible, presenting only a 0.7% field increase in comparison to the phantom alone.

Concerning the dark zones of these four cases, the lowest field regions appear when placing the pad at $d = 0$ mm and $d = 5$ mm for TR1. In the $d = 20$ mm case, the dark zone variations are the lowest on TR1 (only 5% decrease). On TR2, all pads show a similar field variation, only with the first pad presenting a beneficial field increase. Regarding the global SAR and max local SAR of this set, the values on the five cases are relatively similar, showing a slight decrease with increasing distance d.

DISCUSSION

The permittivity of aqueous mixtures of two different perovskite powders was assessed from 50 to 800 MHz, ranging from pure water to completely dry powder. In a first instance, it is important to state that in the whole frequency range, the dielectric values do not vary substantially, as referred to in Webb (26); therefore, a precise analysis was done at 300 MHz—the Larmor frequency of the ^{1}H at 7 T.

A clear structural transition can be seen at a microscopic level in both powders with increasing water content; in a first stage, dry perovskite powder presents itself as disperse particles, quite similar in terms of size and shape. In both perovskite cases, dry particles do not appear to have more than 1 μm of diameter, as can be confirmed by SEM imaging. With increasing water content, particles start forming aggregates as a result of the presence of bound water. When the presence of water

can overcome the porosity of the aggregates, a phase transition occurs and particles form a homogeneous film.

From the permittivity analysis of these perovskite–water mixtures, it is possible to confirm the structural and phase dependency with water content. Therefore, the two structural stages imaged with SEM (aggregate and pasty mixture) can be distinguished in terms of permittivity; an increasing and decreasing dielectric behavior can be seen in the data of Figure 4. First, a large growth occurs in permittivity, from 0%v to 57% v/v for $CaTiO_3$ and 52% v/v for $BaTiO_3$, where ε' and ε'' reach their maximum values. At this point, samples consist of two phases, water and powder, having a pasty consistency. Pressing has no effect on the permittivity of the sample. Thus, a machine-pressed sample falls within the same relative permittivity values as in the manually compressed case.

In the second decreasing stage, in which the sample now consists of three phases (air, water, and powder), from the maximum point until 100% v/v, the relative permittivity for both perovskites decreases notably, until reaching the values of dry powder. It is in this stage in which a significant difference between the manually pressed and machine pressed permittivity occurs for samples having the same water content. In contrast, a shift occurs in the maximal permittivity point, now at 65% v/v for $CaTiO_3$ and 67% v/v for $BaTiO_3$. In the machine-pressed samples just before reaching this point, it appears that flattening the particles by compression expels a fraction of the air trapped in the sample; thus, the permittivity of these points falls within the two-phase Lichtenecker's logarithmic power law (water, powder) model. Nonetheless, after the maximal values, the pressure applied ($2\,tons/cm^2$) was not enough to overcome the influence of the sample's porosity; hence, the permittivity will logically decrease.

The two-phase Lichtenecker's logarithmic power law was shown to correspond to both perovskite permittivity results in the first increasing stage, and therefore in the same value range as in Webb (26). However, the two very different stages found in the data require an adjustment to the used mixing rule, to correctly describe all of the mixture's phases. Therefore, a three-phase CPA law must be applied to the second stage for an accurate adjustment, as three phase components are present: perovskite, water, and a great fraction of air due to the inherent porosity of the powders. It was found that the air and powder fractions originally calculated present a certain uncertainty ($\sim$10%) as a result of the measurement devices used. This intrinsic error was taken into account when calculating the law (Fig. 4b); thus, it is likely that an overestimation of the air fractions was done. When considering a 10% decrease in air fractions, the CPA law corresponds agreeably to the experimental data. If in the case of $BaTiO_3$ this 10% reduction is also considered, the CPA law compares correctly with the data points (Fig. 4b). It is important to highlight how sensitive the CPA law is to a slight change in the porosity fraction, and that all uncertainty needs to be taken into account.

When considering the data in this stage, it appears that by applying a 2-ton/cm^2 pressure to the mixture, permittivity increases by a factor of 4; thus, the permittivity of these mixtures is not only water content–dependent, but also pressure-dependent. In Figure 2d, for a similar water content, the uncompressed spherical $BaTiO_3$ particles are flattened out when applying pressure, thus having a decrease in the overall porosity. In this stage, mixtures are more easily compressed than in the case of dry powder. It appears that with increasing water content, less pressure is required to achieve higher relative permittivity values. The loss tangent of these perovskites is practically constant throughout the water content curve, meaning the amount of water has no influence on the dielectric loss of these mixtures. When reported in the literature, the MRI pads prepared with perovskite-water mixtures do not take the concept of pressure dependency into account, although it could significantly improve dielectric pad performance. There also appears to be a limitation in terms of the highest permittivity achieved for these pads in the literature as a result of saturation of the solution (19,23,26), which we now know can be overcome.

Six pads were prepared to test different configurations on a 7T MRI, and CST Microwave Studio simulations of all of the configurations were achieved. In the first case, Pad A ($\varepsilon' = 62$, 10 mm thick), spaced 1 cm away from the phantom, shows a very subtle effect on B_1^+ field when compared with the control case (phantom without pad). In the second case, a comparison between the fluid Pad B ($\varepsilon' = 219$) and the control case demonstrates a greater effect in the field distribution. Nonetheless, in the third and fourth cases of the highest relative permittivity pads, Pad D ($\varepsilon' = 348$) and Pad F ($\varepsilon' = 475$), the effect in terms of B_1^+ transmit homogeneity appears to be harmful, confirmed by the occurrence of dark zones (i.e., a few regions of low transmit appear, resulting in image artifacts). The red arrows in Figure 6 point to these areas. Figure 6e shows that the dark zone appears to be higher than in the simulation case; this is because of the slightly higher positioning of the pad for scanning. The negative effects of these thick pads indicate that geometry and placement need to be optimized to obtain the best results.

Hence, three sets of pad configurations were assessed. B_1^+ field, global SAR, and local SAR results as a function of pad thickness, pad distance to the head, and pad complex permittivity were evaluated. In terms of pad thickness, a 5-mm pad provides a similar field increase as a 10-mm-thick pad. On TR1 and TR2, the field does not improve in the presence of the 10-mm-thick pad. A $10 + 5$-mm pad shows an extreme field decrease in TR1 and TR2. However, the maximal local SAR for a 10-mm or a $10 + 5$-mm pad is much higher than for a 5-mm pad. Thus, even if not perfectly adapted, a 5-mm pad would be the best compromise. When considering the field generated by the latter pad as a function of distance to the head, the best arrangement would be $d = 0$ mm or $d = 5$ mm, as in these cases the field increase is higher on the CR. Nonetheless, the slightly higher decrease in TR1 should be kept in mind.

Experimentations with a lower permittivity pad of the same dimensions allowed the conclusion that a higher permittivity will contribute to the optimization of the

field distribution. Pad D, when compared with Pad C, induced a 10% higher variation on the coronal average field, but also a 10% field decrease on TR2. Furthermore, the global SAR on the head is similar. The only downside would be an increase in the maximal local SAR; however, by reducing the pad thickness (as in the Pad E case) this issue might be improved. The quantification of these parameters has not been displayed in Figure 10, as it was found that more pads of different permittivities would be needed to validate this set appropriately.

Therefore, the best compromise between B_1^+ field homogeneity and SAR would be Pad E distanced by 0 or 5 mm from the head. This placement shows simultaneously the highest field increase in the coronal region, low decrease in the transversal regions, and a global and maximal local SAR slightly lower than the head phantom without any pad. With a contiguous placement of Pad E, B_1^+ field variation also appears to be beneficial, but the dark zone found on TR1 is significantly higher than for the other distances.

In this study we have performed a $BaTiO_3$ pad assessment of three parameters that we believe are extremely important and can greatly influence field distribution: distance, thickness, and permittivity. Even though the permittivity evaluation was not exhaustive, we believe that some preliminary conclusions were successfully drawn. However, RF shimming pads are extremely complex, and further investigations should be carried out, in terms of reproducibility, evolution over time (because conventional pads have been documented to dry out) (21), and the influence of higher pressures on 60 to 100% v/v mixtures. For instance, another parameter that may influence pad efficiency is the surface of the pad. In this study, all pads were $10 \times 10\,cm^2$, but future work should focus on the variation of this parameter. A few structural changes have been investigated in the literature, such as fluid pad permittivity (by means of simulations) (20) and structural changes for patient comfort improvement (21). These issues should also be considered on the future developments.

The ideal thickness of $BaTiO_3$ pads is nowadays considered to be 5 mm for a relative permittivity of 150 (20), in a configuration contiguous to the patient's head. Nonetheless, polypropylene sealed pads are easily deformed, and the mixture may precipitate over time (21). One of the greatest advantages of these pressed pads is their nondeforming nature, which eliminates the variation in spatial distribution that can take place with fluid pads when they are placed under the patient. Additionally, because these highly pressed mixtures are also nonexpanding, direct molding to the patient's body part of thin pad structures can be considered in the future. Throughout this study, we have used substantial birdcage coils in comparison to the head itself. It was possible to use and place the pads up to 2 cm away from the head. Nonetheless, if these pads were destined to be used with a tight-fitting transceiver array (42), the only possibility would be to mold the pads directly to the patient's features.

As shown by De Heer et al (23), high permittivities such as 475 or 360 greatly benefit body imaging at 3 T. Future work will involve the use of the high permittivity pads prepared in this study for body 3T field-distribution assessment. Additionally, we believe this study could benefit from in vivo experimentation. Therefore, after complete assessment of 3T body field distribution and SAR values, the next step will be system validation by in vivo imaging.

CONCLUSIONS

The influence of water in the dielectric properties of two perovskites powders commonly used nowadays was investigated. Ranging from 0 to 100% v/v of water content, in the frequency range of 50 to 800 MHz, the perovskites $CaTiO_3$ and $BaTiO_3$ present a similar behavior in terms of real and imaginary permittivity. Although the relative permittivity values for $BaTiO_3$ are considerably higher, two stages are differenced as a function of the mixture's water content.

In a first two-phase stage (water and powder), as a result of the decreasing amount of water in the samples, the relative permittivity values of the mixtures tend to increase until reaching a maximal point at approximately 60% v/v. From this point onward, the amount of water present is not enough to overcome the porosity of the samples, causing ε^* values to decrease. Thus, when machine pressing the samples in this stage, and thus expelling the air of the mixture, the phase transition is forced, and it is possible to retrieve a maximal permittivity point even further to the right in the water content curve. The pressure-dependent nature of these mixtures needs to be taken into account in dielectric pad research for high-field MRI.

The ability to control the water–air fraction of the mixture allowed us to obtain superior permittivities than the current state of the art for dielectric pads (19–21).

The pad placement, permittivity, and thickness assessment of higher permittivity pads ($\varepsilon' \geq 350$) demonstrated that thinner pads (5 mm) placed no more than 5 mm away from the head generates the best trade-off between reshaping the B_1^+ field and the global and maximal local SAR induced in the head in the proximity of the pad. Even when not contiguous to the head, pads of this nature are the most promising candidates for dielectric shimming, thus balancing field distribution and SAR effects. Consequently, a single pad can provide the balancing effect needed to correct local B_1^+ defects.

Distancing the pad from the head can be extremely useful in the cases in which the legislation restricts the use of $BaTiO_3$ pads (harmful material if swallowed or inhaled (29)) in direct contact with MRI human volunteers (SVHC according to REACH Regulations EC No. 1907/2006). Otherwise, nontoxic $CaTiO_3$ pads of a new reported maxima ε' 135 may be used contiguous to the head to improve field distribution.

The similarity in the dielectric behavior of both perovskites suggests a structural adjustment in the presence of water that may be extended to other titanate compounds.

ACKNOWLEDGMENTS

REFERENCES

1. Cheng B, Lin YH, Yang H, Lan J, Nan CW, Xiao X, He J. High dielectric permittivity behavior in cu-doped CaTiO3. J Eur Ceram Soc 2009; 92:2776–2779.

2. Haines KN. Applications of high dielectric materials in high field magnetic resonance. Doctoral dissertation: The Pennsylvania State University; 2010.

3. Jing L, Wang G, Duan Y, Jiang Y. Synthesis and electromagnetic characteristics of the flake-shaped barium titanate powder. J Alloys Compd 2009;475:862–868.

4. Wee FH, Malek F, Screekantam S, Al-Amani AU, Ghani F, You KY. Investigation of the characteristics of barium strontium titanate (BST) dielectric resonator ceramic loaded on array antennas. Prog Electromagn Res 2011;121:181–213.

5. Bjorninen T, Babar AA, Ukkonen L, Sydanheimo L, Elsherbeni AZ, Kallioinen J. Compact metal mountable UHF RFID tag on a barium titanate based substrate. Prog Electromagn Res PIER C 2012;26:43–57.

6. Yu P, Cui B, Shi Q. Preparation and characterization of BaTiO3 powders and ceramics by sol–gel process using oleic acid as surfactant. Mat Sci Eng A – Struct 2008;473:34–41.

7. Sadhana K, Krishnaveni T, Praveena K, Bharadwaj S, Murthy SR. Microwave sintering of nanobarium titanate. Scr Mater 2008;59:495–498.

8. Huber C, Treguer-Delapierre M, Elissalde C, Weill F, Maglione M. New applications of the core-shell concept to ferroelectric nanopowders. J Mater Chem 2003;13:650–653.

9. Xiao CJ, Jin CQ, Wang XH. Crystal structure of dense nanocrystalline BaTiO3 ceramics. Mater Chem Phys 2008;111:209–212.

10. Kim CH, Park KJ, Yoon YJ, Sinn DS, Kim YT, Hur KH. Effects of milling condition on the formation of core–shell structure in BaTiO3 grains. J Eur Ceram Soc 2008;28:2589–2596.

11. Ohara S, Kondo A, Shimoda H, Sato K, Abe H, Naito M. Rapid mechanochemical synthesis of fine barium titanate nanoparticles. Mater Lett 2008;62:2957–2959.

12. Wei X, Xu G, Ren Z, Wang Y, Shen G, Han G. Size-controlled synthesis of BaTiO3 nanocrystals via a hydrothermal route. Mater Lett 2008; 62:3666–3669.

13. Fang CY, Wang C, Polotai AV, Agrawal DK, Lanagan MT. Microwave synthesis of nano-sized barium titanate. Mater Lett 2008;62:2551–2553.

14. Hsi CS, Chen YC, Jantunen H, Wu MJ, Lin LC. Barium titanate based dielectric sintered with a two-stage process. J Eur Ceram Soc 2008;28: 2581–2588.

15. Castro J, Rojas E, Ross A, Weller T, Wang J. High-k and low-loss thermoplastic composites for fused deposition modeling and their application to 3D-printed Ku-band antennas. In Proceedings of the Microwave Symposium (IMS), IEEE MTT-S International, San Francisco, CA, USA, 2016. pp 1–4.

16. Alsop DC, Connick TJ, Mizsei G. A spiral volume coil for improved RF field homogeneity at high static magnetic field strength. Magn Reson Med 1998;40:49–54.

17. Wen H, Jaffer FA, Denison TJ, Duewell S, Chesnick AS, Balaban RS. The evaluation of dielectric resonators containing H2O or D2O as RF coils for high-field MR imaging and spectroscopy. J Magn Reson Ser B 1996;110:117.

18. Yang QX, Mao W, Wang J, Smith MB, Lei H, Zhang X, Ugurbil K, Chen K. Manipulation of image intensity distribution at 7.0T: passive RF shimming and focusing with dielectric materials. J Magn Reson Imaging 2006;24:197–202.

19. Haines K, Smith NB, Webb AG. New high dielectric constant materials for tailoring the distribution at high magnetic fields. J Magn Reson 2010;203:323–327.

20. Teeuwisse WM, Brink WM, Haines KN, Webb AG. Simulations of high permittivity materials for 7T neuroimaging and evaluation of a new Barium Titanate-base dielectric. Magn Reson Med 2012;67:912–918.

21. O'Reilly TPA, Webb AG, Brink WM. Practical improvements in the design of high permittivity pads for dielectric shimming in neuroimaging at 7 T. J Magn Reson 2016;270:108–114.

22. Winkler SA, Rutt BK. Practical methods for improving B1 + homogeneity in 3 Tesla breast imaging. J Magn Reson Imaging 2015;41:992–999.

23. De Heer P, Brink WM, Kooij BJ, Webb AG. Increasing signal homogeneity and image quality in abdominal imaging at 3T with very high permittivity materials. Magn Reson Med 2012;68:1317–1324.

24. Brink WM, Van der Jagt AMA, Versluis MJ, Verbist BM, Webb AG. High permittivity dielectric pads improve high spatial resolution magnetic resonance imaging of the inner ear at 7 T. Invest Radiol 2014;49:271–277.

25. Brink WM, Webb AG. High permittivity pads reduce specific absorption rate, improve B1 homogeneity, and increase contrast-to-noise ratio for functional cardiac MRI at 3 T. Magn Reson Med 2014;71:1632–1640.

26. Webb AG. Dielectric materials in magnetic resonance. Concept Magn Reson A 2011;38:148–184.

27. Luo W, Lanagan MT, Sica CT, Ryu Y, Oh S, Ketterman M. Permittivity and performance of dielectric pads with sintered ceramic beads in MRI: early experiments and simulations at 3 T. Magn Reson Med 2013;70:269–275.

28. Calcium Titanate Oxide: MSDS No. 11397. Alfa Aesar website. Accessed April 12, 2016.

29. Barium Titanate Oxide: MSDS No. 12348. Alfa Aesar website. Accessed April 12, 2016.

30. Ba D, Sabouroux P. EpsiMu®, a toolkit for permittivity and permeability measurement in microwave domain at real time of all materials: applications to solid and semisolid materials. Microw Opt Technol Lett 2010;52:2643–2648.

31. Sabouroux P, Ba D. Epsimu, a tool for dielectric properties measurement of porous media: application in wet granular materials characterization. Prog Electromagn Res B 2011;29:191–207.

32. Nicolson AM, Ross GF. Measurement of the intrinsic properties of materials by time-domain techniques. IEEE Trans Instrum Meas 1970; 19:377–382.

33. Georget E, Abdeddaim R, Sabouroux P. A quasi-universal method to measure the electromagnetic characteristics of usual materials in the microwave range. C R Phys 2014;15:448–457.

34. Simpkin R. Derivation of Lichtenecker's logarithmic mixture formula from Maxwell's equations. IEEE Trans Microw Theory Techn 2010; 58:545–550.

35. Sen PN, Scala C, Cohen MH. A self-similar model for sedimentary rocks with application to the dielectric constant of fused glass beads. Geophysics 1981;45:781–795.

36. Buessem WR, Cross LE, Goswami AK. Phenomenological theory of high permittivity in fine-grained barium titanate. J Am Ceram Soc 1966;49:33–36.

37. Ellison WJ. Permittivity of pure water, at standard atmospheric pressure, over the frequency range 0-25 THz and the temperature range 0-100 °C. J Phys Chem Ref Data 2006;36:1–18.

38. Weast R, Astle MJ, Beyer WH. Handbook of chemistry and physics. Boca Raton, FL: CRC Press; 1988. p E-62.

39. Yarnykh VL. Actual flip-angle imaging in the pulsed steady state: a method for rapid three-dimensional mapping of the transmitted radiofrequency field. Magn Reson Med 2007;57:192–200.

40. Brink WM, Versluis MJ, Peeters JM, Börnert P, Webb AG. Passive radiofrequency shimming in the thighs at 3 Tesla using high permittivity materials and body coil receive uniformity correction. Magn Reson Med, 2016;76:1951–1956.

SUPPORTING INFORMATION

Additional Supporting Information may be found in the online version of this article.

Fig. S1. a: The three ROIs outlined in black (coronal plane, Transversal Plane 1, and Transversal Plane 2) considered for B_1^+ field comparison on SAM, displayed here on the B_1^+ field map of the reference scan (without pad). **b**: Simulated coronal, transversal, and sagittal planes of the local SAR of the reference Gustav (without pad).

Table S1. Six Pads Prepared for MRI Testing and Their Full Characteristics
The two gray columns correspond to the uncompressed pads, sealed in a thin polypropylene container.
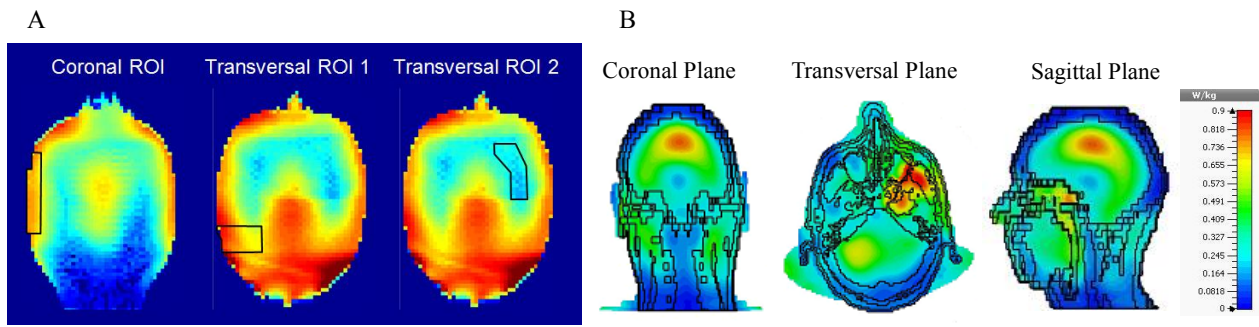
Supporting Figure 11. (A) The three ROIs outlined in black (Coronal plane, Transversal Plane 1 and Transversal Plane 2) considered for B_1^+ field comparison on SAM, displayed here on the B_1^+ field map of the reference scan (without pad); (B) Simulated Coronal, transversal and sagittal planes of the Local SAR of the reference *Gustav* (without pad);

	Pad A	Pad B	Pad C	Pad D	Pad E	Pad F
Water content (v/v)	65.3 %	37.0 %	62.8%	63.1 %	59.8 %	65.3 %
ε'	62	219	241	348	358	475
ε"	5	13	29	58	52	68
Density (g/cm3)	2.07	-	3.68	2.91	3.83	4.03
Thickness	10 mm	10 mm	10 mm	10 mm	5 mm	10 mm

Supporting   Table 1. The six pads prepared for MRI testing and their full characteristics. The two grey columns correspond to the uncompressed pads, sealed in a thin polypropylene container.